RSC Advances

PAPER

View Article Online
View Journal | View Issue

Cite this: *RSC Adv.*, 2018, **8**, 28440

Graphitic carbon-wrapped NiO embedded three dimensional nitrogen doped aligned carbon nanotube arrays with long cycle life for lithium ion batteries

Weina Deng,[a] Xiaohua Chen,*[b] Aiping Hu[b] and Shiying Zhang*[a]

Received 19th April 2018
Accepted 30th July 2018

DOI: 10.1039/c8ra03352h

rsc.li/rsc-advances

In this work, a three-dimensional nitrogen doped aligned carbon nanotube array (NACNTs)@NiO@graphitic carbon composite was fabricated by an effective strategy involving nebulized ethanol assisted infiltration, In this structure, the NiO nanoparticles were wrapped by graphitic carbon layers and NiO@graphitic carbon core–shell nanoparticles adhered strictly to the surface of NACNTs to form a highly ordered 3D structure. When this composite was used as an anode for lithium ion batteries, the well-ordered pore of its NACNTs can facilitate the electrolyte to penetrate and improve electronic conductivity. At the same time, the graphitic layers can promote the stability of a solid electrolyte interface film. Therefore, the NACNTs@NiO@graphitic carbon composite containing 68.1 wt% NiO delivers excellent capacity retention of 91.6% after 200 cycles at 0.2C.

1. Introduction

With the increasing demand for large scale energy storage devices, significant attention has been focused on the development of high energy and power density lithium ion batteries (LIBs). The transition metal oxides (TMOs) such as Fe_2O_3, $NiCo_2O_4$ and NiO have been investigated as the anode electrode in LIBs because of their high energy density and natural abundance. Among them, with high theoretical specific capacity (718 mA h g^{-1}), low cost and environmental benignity, NiO has attracted great attention.[1–6] However, the practical application of NiO-based materials as the anode for LIBs is impeded mainly by its poor capacity retention because of the huge volume change during lithiation/delithiation processes, resulting in severe pulverization of the NiO particles. In addition, the compromise of rate capability is another serious concern because NiO is too insulating to support fast electron transport for charge/discharge at high rates.[7–10] To alleviate these problems, an effective strategy is to fabricate NiO with different morphologies such as nanoparticles,[11] nanosheets,[12–14] nanospheres[15,16] and nanoflowers[4] shortening the Li^+ diffusion path to alleviate the pulverization of active materials. Hybridizing NiO with carbon to improve the Li^+ storage properties and the overall electronic conductivity is another strategy.[8,12,14,17,18] Up to now, carbon nanotubes (CNTs),[13,16,19] graphene,[20–23] ordered mesoporous carbon (CMK-3),[14] amorphous carbon[8,12] and carbon fiber[24,25] are often used to build carbon/NiO nanostructure. Among these options, CNTs are of particular interest because of their favorable structure flexibility, large specific surface area, good electrolyte accessibility and excellent electrical conductivity.[26] Furthermore, when combining NiO with CNTs, the NiO can increase the available surface area of CNTs, which can contribute to the high electrochemical activity. In addition, the CNTs can induce the nucleation, growth and formation of NiO on their surface.[12] Unfortunately, the actual lithium storage performance of the CNTs-based materials is much lower than the expected value because of the weak interfacial interaction between active materials and CNTs. Liu and co-works[13] demonstrate that the doped N can improve the interaction between active material and N doped CNTs (NCNTs), and facilitate the electron hopping from NCNTs to active material, subsequently, promoting the electronic conductivity of NCNTs-based composite material. Furthermore, Z. Yang reported that the aligned NCNTs (NACNTs) exhibit significantly improved charge transport capability and electrolyte accessibility owing to the well 1D directed conductive electron channel and the well-ordered pore structure.[27] Therefore, the NACNTs have been intensively investigated as energy storage devices such as lithium-ion battery[28–32] and supercapacitor.[33–36] It is expected that the NACNTs as a support material will show better electrochemical properties than random CNTs.

In addition, recent studies demonstrate that the formation of a thick and unstable solid electrolyte interface (SEI) film on TMOs electrode causes consumption of abundant Li^+ during

[a]Hunan Key Laboratory of Applied Environmental Photocatalysis, Changsha University, Changsha 410022, China. E-mail: cszhangsy@ccsu.edu.cn; Tel: +86-731-84261297

[b]College of Materials Science and Engineering, Hunan University, Changsha 410082, China. E-mail: xiaohuachen@hnu.edu.cn

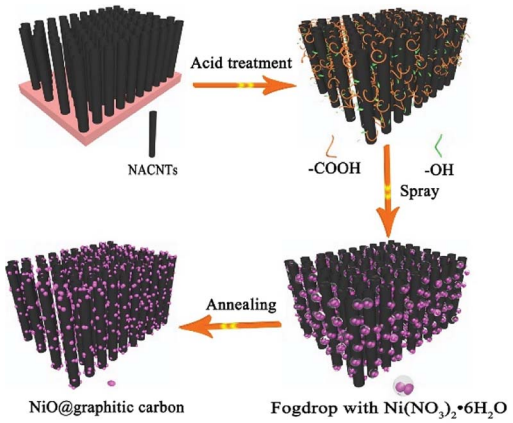

Fig. 1 Schematic diagram of the synthesis procedure for NACNTs@-NiO@graphitic carbon composite.

cycles, which lead to a high irreversibility loss of capacities.[37] In order to solve the above problem and improve the structural stability, much effort has been developed to fabrication of carbon-coated TMOs composites in which the SEI films being formed on the surface of coated carbon are relatively stable. The TMOs nanostructures with a coated carbon layer can also maintain their original morphology by protecting TMOs from direct contacting with the electrolyte so as to avoid the pulverization resulting from the repeated lithiation/delithiation and improve cycling stability.[38,39]

In this work, a 3D NACNTs@NiO@graphitic carbon composite was fabricated with the help of ethanol-assisted infiltration and nebulizing action. In this structure, NiO nanoparticles were wrapped by graphitic carbon generated from the ethanol thermal decomposition, and the NiO@graphitic carbon particles were deeply and uniformly dispersed on the surface of NACNTs. The nebulization action could significantly decrease the size of the nickel nitrate droplets, and was beneficial to the infiltration of nickel nitrate embed into the NACNTs. Fig. 1 shows the synthetic process of the NACNTs@NiO@graphitic carbon composite formation. Firstly, the as-prepared NACNTs were purified with maintaining the 3D alignment by being immersed in nitric acid. The purification was used to remove the surplus catalyst particles and introduce oxygen containing functional groups (–OH and –COOH) which was helpful for absorption of inorganic groups. Secondly, the $Ni(NO_3)_2 \cdot 6H_2O$ ethanol solution was nebulized into the inter-tube spaces with some NACNTs at room temperature through the ultrasonic nebulizer. Finally, NiO nanoparticles formed in the NACNTs *via* the pyrolysis reaction of the $Ni(NO_3)_2 \cdot 6H_2O$ at 400 °C. At the same time, graphitic carbon layers coated on NiO surface were fabricated with NiO as catalyst and ethanol as carbon-source.[40,41]

2. Experiments

All solvents and chemicals were of analytical reagent grade and obtained from Sinopharm Chemical Reagent, China.

2.1 Preparation of NACNTs@NiO@graphitic carbon composites

3D NACNTs were prepared as our previous report.[42] 0.8 g ferrocene was ultrasonically dissolved in a mixed solvent with 26 ml xylene and 14 ml cyclohexylamine. The reaction solution was atomized by an ultrasonic nebulizer and passed into the quartz tube, in which a quartz slice (3 mm × 30 mm × 30 mm) was used as a substrate for the NACNTs at a temperature of 900 °C with argon as the carrier gas. The as-synthesized NACNTs were immersed into nitric acid at 120 °C for 9 h, washed with deionized water until it was neutral and then dried in vacuum at 80 °C overnight.

In a typical synthesis of NACNTs@NiO@graphitic carbon, 40 ml ethanol solution containing 2 mmol $Ni(NO_3)_2 \cdot 6H_2O$ was nebulized to a mist of droplets which infiltrate into the obtained NACNTs at room temperature with argon carrying gas at a flow rate of 600 sccm. After that, the resulting samples were heated for 2 h at 400 °C under an air atmosphere. After being cooled naturally, it was washed with ethanol and deionized water and dried at 80 °C under vacuum overnight. The resulting materials are denoted as NACNTs@NiO@G-20, NACNTs@NiO@G-30 and NACNTs@NiO@G-40, according to the nebulization time.

2.2 Materials characterization

The morphology, size and intrinsic structure of the samples were characterized by field emission scanning electron microscope (SEM, Hitachi S4800, 30 kV) and transmission electron microscope (TEM, JEM-2100F, 200 kV). The crystal structures of the samples were characterized by X-ray diffraction (XRD) on a Bruker D8 Advance X-ray diffractometer with Cu Kα radiation (λ = 0.15418 nm). The contents of NiO were carried out by thermogravimetric analysis (TGA, TG/DTA7300) with a heating rate of 5 °C min^{-1} in flowing air atmosphere from room temperature to 700 °C. X-ray photoelectron spectroscopy (XPS) analysis was performed using a K-Alpha 1063 (Thermo Fisher Scientific, UK).

2.3 Electrochemical characterization

The electrochemical performance tests were performed under ambient temperature conditions, using CR2025-type coin cells assembled with lithium foils as the counter electrodes in a high purity argon filled glove box. The working electrode consisted of active materials, carbon black and polyvinylidene fluoride (PVDF, Aldrich) with a 80 : 10 : 10 weight ratio in *N*-methylpyrrolidone (NMP) with constant stirring for 8 h to form a homogeneous slurry. Then the well-mixed slurry was spread onto a copper foil and dried at 80 °C in a vacuum oven for 12 h. A Celgard 2300 microporous polypropylene membrane was used as a separator and the utilized electrolyte was a solution of 1 M $LiPF_6$ in ethylene carbonate/dimethyl carbonate (1 : 1 in volume). The charge/discharge tests were performed on a Land CT2001A battery test system (Wuhan, China). Cyclic voltammetry and electrochemical impedance spectroscopy measurements (EIS) were performed on an electrochemical workstation (CHI660D).

3. Results and discussion

3.1 Morphology and structure characterization

The morphology of the prepared NACNTs and NACNTs@NiO@graphitic carbon composites was firstly studied by scanning electron microscope (SEM) in Fig. 2. It can be seen that large-area NACNTs still maintain the good alignment after NiO particles embedded. Such aligned CNTs and their regular pore structure could provide short diffusion pathways for Li^+ and electronic transport, which are greatly beneficial for the electrochemical performance. As shown in Fig. 2b–d, the NiO particles anchored on the surface of the NACNTs homogeneously owing to the interaction between oxygen containing functional groups and NiO particles, and the number of NiO nanoparticles mainly depends on the duration of the nebulization. With increasing the nebulization time, the number of NiO nanoparticles increases, and the particles size remains similar. When the nebulization time increases to 40 min, the NiO particles aggregate each other, which may provide complicate pathways for Li^+ to the NiO nanoparticles and thus making it difficult for electrolyte penetration.

From the transmission electron microscopy (TEM) images (Fig. 3), it can be clearly observed that the as-obtained NiO with the size around 30 nm was wrapped by some graphitic carbon layers (marked by arrow), which could be distinctly observed in the subsequent HRTEM. In the NACNTs@NiO@G-20 and NACNTs@NiO@G-30 samples (Fig. 3a and b), the NiO nanoparticles uniformity distributed on the surfaces of NACNTs. Increasing nebulization time to 40 min, NiO nanoparticles featured observably overlapping and aggregating (Fig. 3c). The HRTEM image of NACNTs@NiO@G-30 shows that the lattice fringe with an interplanar spacing of 0.24 nm is consistent with the (111) planes of NiO (Fig. 3d). In addition, it can also be obviously examined that some graphitic layers, with the interplanar distance of 0.34 nm, wrapped on NiO particle surface. The graphitic carbon layers can promote the formation of stable SEI film and reduce the consumption of some Li^+. It is expected that the graphitic carbon layers will be beneficial to achieve superior cycling stability.

Fig. 4a shows the XRD patterns of the NACNTs, NACNTs@NiO@G-20, NACNTs@NiO@G-30, NACNTs@NiO@G-40 and NiO. A broad diffraction peaks at around 26° can be indexed to (002) planes of NACNTs and the peak intensities decreased with increasing the nebulization time, owing to the increase of the NiO nanoparticles coated on the surface of the NACNTs. The diffraction peaks at 37°, 43°, 62°, 75° and 79° can be indexed to (111), (200), (220), (311) and (222) planes of the crystalline NiO, respectively.

The NiO content of the composite was determined through the TGA carried out from room temperature to 700 °C with a heating rate of °C min^{-1} in air atmosphere. As shown in Fig. 4b, a first mass loss was noticed in the range of 30–200 °C, which is mainly due to the release of traces of absorbed water. A sharp mass loss was detected at 400–600 °C and it is attributed to the combustion of the NACNTs and graphitic carbon. According to

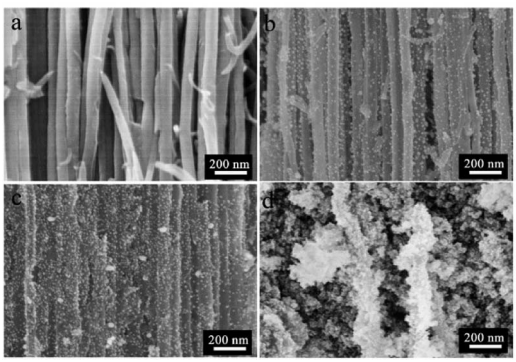

Fig. 2 SEM images of NACNTs (a); NACNTs@NiO@G-20 (b); NACNTs@NiO@G-30 (c) and NACNTs@NiO@G-40 (d).

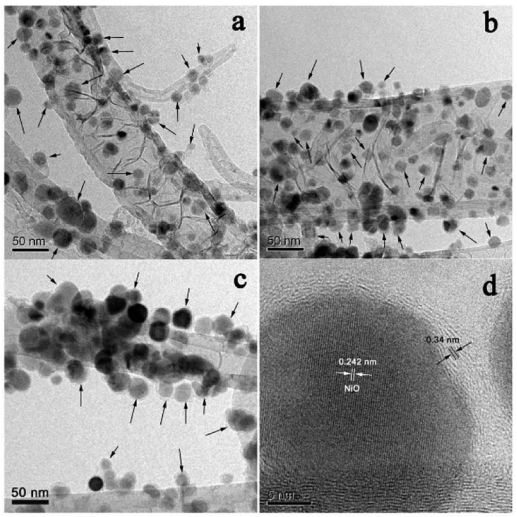

Fig. 3 TEM images of NACNTs@NiO@G-20 (a); NACNTs@NiO@G-30 (b) and NACNTs@NiO@G-40 (c). HRTEM image of the individual NiO nanoparticles from sample NACNTs@NiO@G-30 (d).

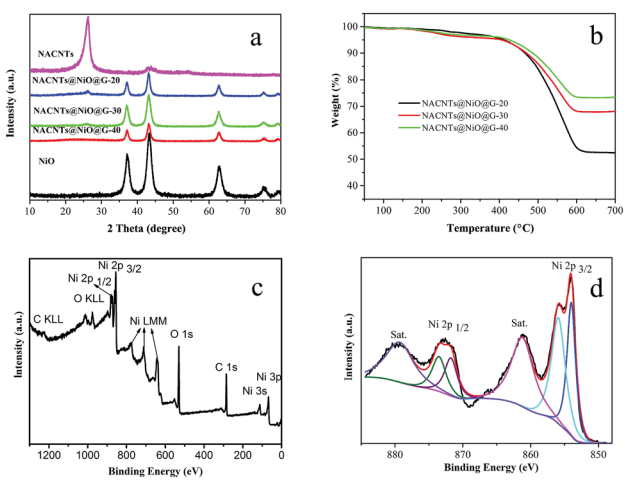

Fig. 4 (a) XRD patterns of NACNTs, NACNTs@NiO@G-20, NACNTs@NiO@G-30, NACNTs@NiO@G-40 and NiO; (b) TGA curve of the NACNTs@NiO@G-20, NACNTs@NiO@G-30, NACNTs@NiO@G-40 composites; (c) XPS spectra of the surface chemical composition of NACNTs@NiO@G-30 composite; (d) Ni 2p XPS spectra of the NACNTs@NiO@G-30 composite.

calculations, the NiO contents of NACNTs@NiO@G-20, NACNTs@NiO@G-30, NACNTs@NiO@G-40 are estimated to be around 52.5%, 68.1% and 73.5% by weight, respectively.

X-ray photoelectron spectroscopy (XPS) is used to further investigate the detailed elemental composition and the valence states of the NACNTs@NiO@G-30, and the corresponding wide range spectrum is presented in Fig. 4c. The full spectrum of NACNTs@NiO@G-30 indicates the presence of carbon (C 1s), oxygen (O 1s), nitrogen (N 1s) and Ni. In the Ni 2p region (Fig. 4d), the peaks at 854.1.1 eV and 855.9 eV with its satellite peak at 861.2 eV were ascribed to the Ni $2p_{3/2}$. The peaks located at 871.8 and 873.5 eV combining with a satellite peak at 879.3 eV are the Ni $2p_{1/2}$.

The peak positions and shapes imply that the characteristic peaks of Ni–O bonds mainly exists, which indicates that Ni element mainly exists in the form of Ni^{2+}.

3.2 Electrochemical performance

The electrochemical performance of NACNTs@NiO@graphitic carbon as anode materials for LIBs was investigated in the voltage window of 0.01–3.0 V at room temperature based on the mass of NACNTs@NiO@graphitic carbon composite (Fig. 5). Cyclic voltammetry (CV) test for the first three cycles was carried out to elucidate the redox processes of NACNTs@NiO@graphitic carbon electrode (Fig. 5a). In the first cathodic scan, the irreversible peak is located at around 0.42 V, which originate from the initial reduction of Ni^{2+} to Ni^0 as well as the formation of the solid electrolyte interface (SEI) layer on the surface of electroactive materials.[43,44] In the subsequent anodic scan, a peak at around 2.26 V can be obviously observed, which is normally assigned to the reversible oxidation of NiO to Ni^{2+} and decomposition of Li_2O to Li.[45,46] While the peak at 1.55 V is associated with the partial decomposition of the SEI layer. The cathodic peak shifts to about 1.0 and the anodic peak to 2.36 V for the subsequent cycles due to the drastic lithium-driven structural or textural modifications.[47] The CV curves are quite similar after the first cycle, suggesting a good electrochemical reversibility and a cyclic stability of the synthesized NACNTs@NiO@graphitic carbon electrode.

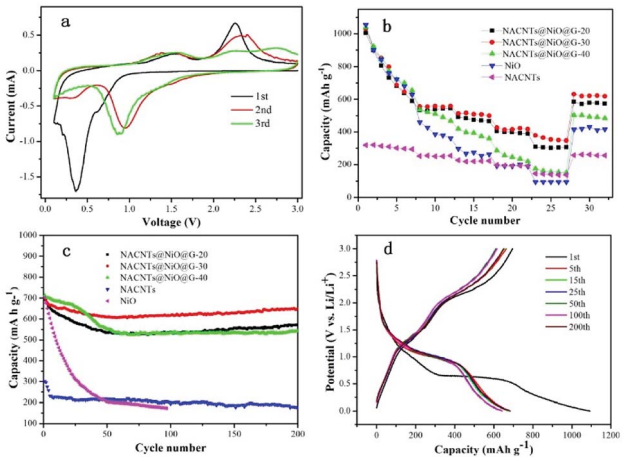

Fig. 5 (a) The first three CV curves of the NACNTs@NiO@G-30 electrode at a scan rate of 0.1 mV s^{-1}; (b) rate performance of NACNTs@NiO@G-20, NACNTs@NiO@G-30, NACNTs@NiO@G-40, NiO and NACNTs at various current rates; (c) cycling performance of the electrodes made from NACNTs@NiO@G-20, NACNTs@NiO@G-30, NACNTs@NiO@G-40, NiO and NACNTs at 0.2C current rate; (d) charge/discharge curves of the NACNTs@NiO@G-30 electrode 0.2C current rate.

The rate performances of NACNTs@NiO@graphitic carbon are evaluated by galvanostatic charge/discharge cycling at different rates. For comparison, we measured NACNTs and pure NiO synthesized by hydrothermal method under the same test condition (Fig. 5b). It can be obviously observed that the charge/discharge capacity decreases with the rate increasing and the NACNTs@NiO@G-30 electrode shows the best rate performance among all samples. Its discharge specific capacities in the first cycle are 1030, 559, 507, 425, 383 and 630 mA h g^{-1} at the rate of 0.1, 0.2, 0.5, 1, 2 and 0.1C, respectively, and the coulombic efficiencies sustained over 95% during each cycling. The NACNTs, NiO, NACNTs@NiO@G-20 and NACNTs@NiO@G-40 cathodes exhibit lower specific capacities at each rate stages than NACNTs@NiO@G-30 and retained specific capacities of only 146, 95, 308, and 173 mA h g^{-1} at 2C with specific capacities of 319, 1054, 1003 and 1039 mA h g^{-1} for the first cycle, respectively. According to the compositions of sample and the theoretical specific capacity of NiO (718 mA h g^{-1}) and CNTs (345 mA h g^{-1}), the theoretical capacity of the active material strongly depends on the NiO fraction. The theoretical capacity was calculated in the following section:

$$C_{\text{Theoretical}} = C_{\text{NiO}} \times \%_{\text{mass of NiO}} + C_{\text{CNTs}} \times \%_{\text{mass of CNTs}}$$

It can be obviously known that the theoretical capacity of the active material increases with the increasing of NiO fraction. Unfortunately, when the nebulization time increases to 40 min, the transport channels for electron and Li^+ to the agglomerated particles become more complicated, which makes the electrolyte penetrate into the inner part of active materials more difficult, thus leading to the decrease of the specific capacity. To determine the effect of NiO amount on the electrochemical properties, we test the cycle performance of various NACNTs@NiO@graphitic samples up to 200 cycles at the current rate of 0.2C. Moreover, pure NiO sample and NACNTs were also investigated under the same conditions. As shown in Fig. 5c, it can be seen that NACNTs@NiO@graphitic carbon composites exhibit better cycle stability compared to NACNTs or pure NiO. The NACNTs@NiO@G-30 electrode delivers the best electrochemical properties. It exhibits a capacity of 708 mA h g^{-1} for the first cycle and above 95% coulombic efficiency after the first five cycles with maintaining capacities of 624 mA h g^{-1} for the 70th cycle. While, the NACNTs@NiO@G-20 electrode and the NACNTs@NiO@G-40 electrode exhibit capacities of 693, 713 mA h g^{-1} for the first cycle with retaining capacities of 533 and 525 mA h g^{-1} for the 70th cycle, respectively. Interestingly, with the discharging and charging going on, the specific capacities of all NACNTs@NiO@graphitic

carbon composites electrodes increase gradually and reach a value as high as 649 mA h g^{-1}, 571 mA h g^{-1} and 543.2 mA h g^{-1} at the 200th cycle, respectively. These results can be ascribed to the electrochemical activation process during the cycle process, which is commonly observed for transition metal oxides electrodes.[21,48–50]

In addition, it should be noted that when using pure NiO or NACNTs separately as the electrode, they exhibit very low discharge capacities of 64 and 202 mA h g^{-1} respectively. This indicates that our strategy is very beneficial for promoting the cycling stability of the NiO-based active material. Fig. 5d depicts the charge/discharge voltage profiles of the NACNTs@NiO@G-30 cathode at different cycle (1, 5, 15, 25, 50, 100 and 200) at 0.2C. It can be observed that the first charge profile exhibits a well-defined discharge plateau between 0.65 V and 0.55 V, while the plateaus in the following cycles become less obvious and located between 1.05 V and 0.90 V. This result agrees well with that of the CV measurement and finally delivers a capacity of 1092 mA h g^{-1}. For NACNTs@NiO@G-30 electrode, an initial discharge capacity of 695 mA h g^{-1} is achieved with an initial coulombic efficiency of 64%. Its irreversible capacity loss can be explained by the formation of SEI layer on the surface of active material and the irreversible lithium insertion reaction, which is a common phenomenon for most anode materials.[51] Furthermore, a discharge capacity of 702 mA h g^{-1}, 665 mA h g^{-1}, 654 mA h g^{-1}, 651 mA h g^{-1} and 609 mA h g^{-1} is achieved in the 5th, 15th, 25th, 50th and 100th cycle. With the electrochemical cycles going on, the capacity fade is minimal. Up to the 200th cycle, a capacity of 649 mA h g^{-1} with a coulombic efficiency of 95.2% maintained and a capacity retention of 91.6% is achieved. The outstanding stability results from our novel structure, in which the electronic conductivity of active materials can be improved and the pulverization and aggregation of NiO can be prevented.

It is worth noting that the NACNTs@NiO@G-40 electrode exhibits a higher discharge capacity than that of the other electrode during the initial 30 cycles, which may be due to the fact that the theoretic specific of NiO (718 mA h g^{-1}) is higher than that of NACNTs and the theoretical specific capacity of NACNTs@NiO@ graphitic carbon composite increases with the nebulization time. After 30 cycles, the NACNTs@NiO@G-30 electrode shows the highest discharge capacity. In order to explain this phenomenon, electrochemical impedance spectroscopy (EIS) measurements were performed for the NACNTs@NiO@G-30 and NACNTs@NiO@G-40 electrodes after different cycles at 0.2C. Fig. 6 shows the Nyquist plots for the two electrodes, which consist of a depressed semicircle in the high and middle frequency regions and an inclined line in the low-frequency region. The high frequency semicircle can be assigned to the contact resistance caused by formation of SEI layer (R_{SEI}), while the middle frequency semicircle is attributed to the charge-transfer impedance on electrode–electrolyte interface (R_{ct}). The linear region represents typical Warburg behavior, reflecting the solid state diffusion of Li^+ into the active materials. As can be observed, the fresh cells show the lowest values of the combined R_{SEI} and R_{ct} for the both electrodes, confirming the existence of SEI layer after the first charge/discharge process. Moreover, it can be obviously observed that the value of R_{SEI} and R_{ct} of NACNTs@NiO@G-40 electrode is always higher than that of NACNTs@NiO@G-30. This is due to the comparatively high NiO content for NACNTs@NiO@G-40, which results in a decrease in the interfacial area between the NACNTs and the electrolyte, thus increasing the resistance. Besides, with increasing the content of NiO in the composite, the transport pathways for electron and Li^+ to the NiO particles become more complicated in NACNTs@NiO@G-40 electrode, resulting in the inaccessible for electrolyte penetration to the active materials. The result is consistent with the cycling performance tests of the two electrodes.

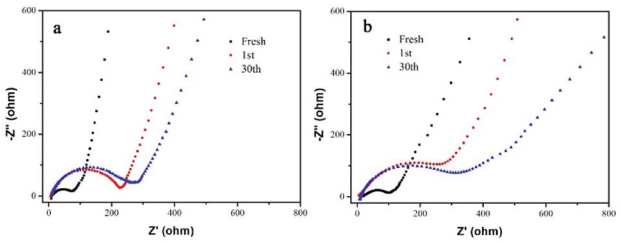

Fig. 6 (a) EIS of NACNTs@NiO@G-30 electrode after different cycles; (b) EIS of NACNTs@NiO@G-40 electrode after different cycles.

Fig. 7 is the schematic illustration of electron transfer and the Li^+ diffusion on the 3D NACNTs@NiO@graphitic carbon. The outstanding electrochemical performance of the NACNTs@NiO@G-30 composites can be attributed to several aspects. ① The 1D directed conductive electron paths of NACNTs ensures the excellent electronic conductivity of integral electrode; ② the well-ordered pore structure can not only promote the penetration of electrolyte into the active materials and shorten the Li^+ diffusion length, but also allow the efficient electrolyte transport throughout the active materials; ③ the coated graphitic layer improves the structural stability by protecting NiO from directly contacting with electrolyte and facilitate the formation of the stable SEI layer. Due to the combination effect of these factors, the 3D NACNTs@NiO@graphitic carbon electrode shows excellent electrochemical properties.

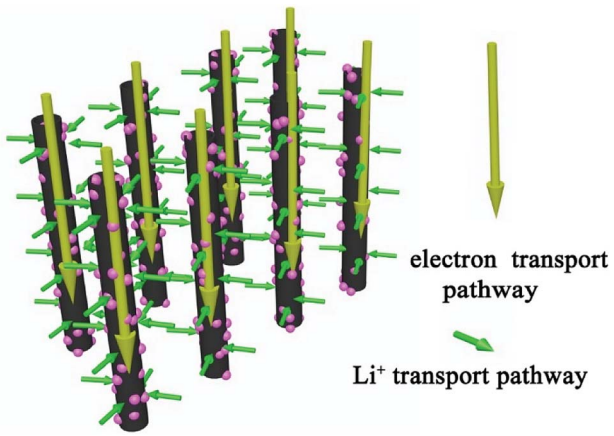

Fig. 7 Schematic illustration of electron and Li^+ transport pathway for NACNTs@NiO@graphitic carbon composite.

Conclusions

In summary, 3D NACNTs@NiO@graphitic carbon composites were successfully synthesized with the help of nebulizing action followed by calcination at air and used as anode materials for LIBs. In this structure, well-ordered pore structure combined with well 1D directed conductive electron channels of NACNTs provided the shortest transport pathways for electron and Li^+. The coated graphitic carbon layer on the surface of NiO nanoparticles prevents the direct contact between NiO and electrolyte and also alleviates pulverization of NiO during the lithiation/delithiation processes. A capacity of 649 mA h g^{-1} at a current density of 0.2C after 200 cycles is achieved for NACNTs@NiO@G-30. In view of this, NACNTs@NiO@graphitic carbon composites might serve as a promising candidate for next generation lithium-ion batteries.

Conflicts of interest

There are no conflicts to declare.

Acknowledgements

This work was financially supported by the Natural Science Foundation of Hunan Province, China (No. 2018JJ3559), Scientific Research Project of Education Department of Hunan Province (No. 16C0131) and Science and Technology Plan Projects of Changsha (No. ZD1601072).

References

1 L. Gu, W. Xie, S. Bai, B. Liu, S. Xue, Q. Li and D. He, *Appl. Surf. Sci.*, 2016, **368**, 298–302.
2 M. Chen, X. Xia, M. Qi, J. Yuan, J. Yin and Q. Chen, *Electrochim. Acta*, 2015, **184**, 17–23.
3 H. S. Jadhav, G. M. Thorat, J. Mun and J. G. Seo, *J. Power Sources*, 2016, **302**, 13–21.
4 Y. P. Pang, J. Zhang, D. R. Chen and X. L. Jiao, *RSC Adv.*, 2016, **6**, 30395–30400.
5 T. Li, S. Ni, X. Lv, X. Yang and S. Duan, *J. Alloys Compd.*, 2013, **553**, 167–171.
6 Q. Q. Xiong, J. P. Tu, X. H. Xia, X. Y. Zhao, C. D. Gu and X. L. Wang, *Nanoscale*, 2013, **5**, 7906–7912.
7 Y. Xia, W. Zhang, Z. Xiao, H. Huang, H. Zeng, X. Chen, F. Chen, Y. Gan and X. Tao, *J. Mater. Chem.*, 2012, **22**, 9209–9215.
8 Y. Feng, H. Zhang, W. Li, L. Fang and Y. Wang, *J. Power Sources*, 2016, **301**, 78–86.
9 X. Huang, J. Tu, C. Zhang and F. Zhou, *Electrochim. Acta*, 2010, **55**, 8981–8985.
10 Y. Yang, J. Liu, H. Dai, Y. Cui, J. Liu, X. Liu and Z. Fu, *J. Alloys Compd.*, 2016, **661**, 190–195.
11 A. K. Mondal, D. Su, Y. Wang, S. Chen, Q. Liu and G. Wang, *J. Alloys Compd.*, 2014, **582**, 522–527.
12 X. Xu, H. Tan, K. Xi, S. Ding, D. Yu, S. Cheng, G. Yang, X. Peng, A. Fakeeh and R. V. Kumar, *Carbon*, 2015, **84**, 491–499.
13 J. Wu, W. Yin, W. Liu, P. Guo, G. Liu, X. Liu, D. Geng, W. M. Lau, H. Liu and L. Liu, *J. Mater. Chem.*, 2016, **4**, 10940–10947.
14 Z. Fan, J. Liang, W. Yu, S. Ding, S. Cheng, G. Yang, Y. Wang, Y. Xi, K. Xi and R. V. Kumar, *Nano Energy*, 2015, **16**, 52–162.
15 Z. bai, Z. Ju, C. Guo, Y. Qian, B. Tang and S. Xiong, *Nanoscale*, 2014, **6**, 3268–3273.
16 P. Lv, H. Zhao, Z. Zeng, C. Gao, X. Liu and T. Zhang, *Appl. Surf. Sci.*, 2015, **329**, 301–305.
17 Y. W. Li, Y. Y. Zheng, J. H. Yao, J. R. Xiao, J. W. Yang and S. H. Xiao, *RSC Adv.*, 2017, **7**, 31287–31297.
18 X. Wang, L. Zhang, Z. Zhang, A. Yu and P. Wu, *Phys. Chem. Chem. Phys.*, 2016, **18**, 3893–3899.
19 Y. Ma, L. Sheng, H. Zhao, K. An, L. Yu, J. Xu and X. Zhao, *Solid State Sci.*, 2015, **46**, 49–55.
20 S. G. Hwang, G. O. K. Kim, S. R. Yun and K. S. Ryu, *Electrochim. Acta*, 2012, **78**, 406–411.
21 C. Kang, E. Cha, S. H. Lee and W. B. Choi, *RSC Adv.*, 2018, **8**, 7414–7421.
22 C. Chen, P. J. Perdomo, M. Fernandez, A. Barbeito and C. Wang, *Journal of Energy Storage*, 2016, **8**, 198–204.
23 Y. J. Mai, S. J. Shi, D. Zhang, Y. Lu, C. D. Gu and J. P. Tu, *J. Power Sources*, 2012, **204**, 155–161.
24 Z. Wang, M. Zhang and J. Zhou, *ACS Appl. Mater. Interfaces*, 2016, **8**, 11507–115015.
25 Y. Wei, F. Yan, X. Tang, Y. Luo, M. Zhang, W. Wei and L. Chen, *ACS Appl. Mater. Interfaces*, 2015, **7**, 21703–21711.
26 E. Frackowiak and F. Béguin, *Carbon*, 2002, **40**, 1775–1787.
27 Z. Yang, X. Zhou, Z. Jin, Z. Liu, H. Nie, X. Chen and S. Huang, *Adv. Mater.*, 2014, **26**, 3156–3161.
28 L. G. Bulusheva, A. V. Okotrub, A. G. Kurenya, H. Zhang, H. Zhang, X. Chen and H. Song, *Carbon*, 2011, **49**, 4013–4023.
29 Y. Wu, Y. Wei, J. Wang, K. Jiang and S. Fan, *Nano Lett.*, 2013, **13**, 818–823.
30 S. Li, Y. Luo, W. Lv, W. Yu, S. Wu, P. Hou, Q. Yang, Q. Meng, C. Liu and H. M. Cheng, *Adv. Energy Mater.*, 2011, **1**, 486–490.
31 A. Gohier, B. Laïk, K. H. Kim, J. L. Maurice, J. P. Pereira-Ramos, C. S. Cojocaru and P. T. Van, *Adv. Mater.*, 2012, **24**, 2592.
32 W. Wang, R. Epur and P. N. Kumta, *Electrochem. Commun.*, 2011, **13**, 429–432.
33 Y. Zhou, H. Xu, N. Lachman, M. Ghaffari, S. Wu, Y. Liu, A. Ugur, K. K. Gleason, B. L. Wardle and Q. M. Zhang, *Nano Energy*, 2014, **9**, 176–185.
34 M. Ghaffari, S. Kosolwattana, Y. Zhou, N. Lachman, M. Lin, D. Bhattacharya, K. K. Gleason, B. L. Wardle and Q. M. Zhang, *Electrochim. Acta*, 2013, **112**, 522–528.
35 R. Amade, E. Jover, B. Caglar, T. Mutlu and E. Bertran, *J. Power Sources*, 2011, **196**, 5779–5783.
36 A. L. Reddy, M. M. Shaijumon, S. R. Gowda and P. M. Ajayan, *Nano Lett.*, 2009, **9**, 1002–1006.
37 F. Han, D. Li, W. C. Li, C. Lei, Q. Sun and A. H. Lu, *Adv. Funct. Mater.*, 2013, **23**, 1692–1700.
38 H. Zhang, L. Zhou, O. Noonan, D. J. Martin, A. K. Whittaker and C. Yu, *Adv. Funct. Mater.*, 2014, **24**, 4337–4342.

39 C. Lei, F. Han, D. Li, W. C. Li, Q. Sun, X. Q. Zhang and A. H. Lu, *Nanoscale*, 2013, **5**, 1168–1175.
40 H. E. Unalan and M. Chhowalla, *Nanotechnology*, 2005, **16**, 2153–2163.
41 A. N. Andriotis, M. Menon and G. Froudakis, *Phys. Rev. Lett.*, 2000, **85**, 3193–3196.
42 W. Deng, X. Chen, X. Chen, Z. Liu, Y. Zeng, A. Hu, Y. Xiong, Z. Li and Q. Tang, *Nanotechnology*, 2014, **25**, 475601.
43 D. Xie, Q. Su, Z. Dong, J. Zhang and G. Du, *CrystEngComm*, 2013, **15**, 8314–8319.
44 X. H. Huang, J. P. Tu, C. Q. Zhang and F. Zhou, *Electrochim. Acta*, 2010, **55**, 8981–8985.
45 Y. Shi, B. Guo, S. A. Corr, Q. Shi, Y. S. Hu, K. R. Heier, L. Chen, R. Seshadri and G. D. Stucky, *Nano Lett.*, 2009, **9**, 4215–4220.
46 X. Sun, W. Si, X. Liu, J. Deng, L. Xi, L. Liu, C. Yan and O. G. Schmidt, *Nano Energy*, 2014, **9**, 168–175.
47 P. Poizot, S. Laruelle, S. Grugeon, L. Dupont and J. M. Tarascon, *Nature*, 2000, **407**, 496.
48 X. Xu, Z. Fan, X. Yu, S. Ding, D. Yu and X. W. Lou, *Adv. Energy Mater.*, 2015, **4**, 1400902.
49 Z. Wang, D. Luan, S. Madhavi, Y. Hu and X. W. Lou, *Energy Environ. Sci.*, 2012, **5**, 5252–5256.
50 G. Zhang, L. Yu, H. B. Wu, H. E. Hoster and X. W. Lou, *Adv. Mater.*, 2012, **24**, 4609–4613.
51 X. Wang, Z. Yang, X. Sun, X. Li, D. Wang, P. Wang and D. He, *J. Mater. Chem.*, 2011, **21**, 9988–9990.